

**Effect of Inhibitor Concentration on the Adsorption and Inhibition Mechanism for Mica and Carbon Steel Studied by *In Situ* Atomic Force Microscopy**

H. Wang, B. Brown, S. Nestic  
Institute for Corrosion Multiphase Technology  
Department of Chemical & Biomolecular Engineering, Ohio University  
342 West State Street  
Athens, OH 45701  
USA

A. Pailleret  
Sorbonne Université, CNRS, Laboratoire Interfaces et Systèmes Electrochimiques (LISE, UMR 8235)  
4 place Jussieu, (case courrier 133)  
Paris, 75005  
France

**ABSTRACT**

In the oil and gas industry, carbon steel is widely used in the construction of infrastructure, such as pipelines and tanks, for the transmission and storage of crude oil as well as petroleum products. This is due to its excellent mechanical properties, ease to work with, and low cost. However, it is vulnerable to corrosion. Ionic surfactant type of corrosion inhibitors have been widely applied against pipeline corrosion due to their high mitigation efficiency at low applied concentrations. Corrosion inhibition efficiency is closely related to the inhibitor adsorption mechanism. However, past corrosion inhibition research has generally focused on the electrochemical mechanisms of inhibition processes and associated corrosion rate reductions. In this current work, *in situ* tapping mode AFM phase imaging and contact mode AFM nano-scratching techniques have been applied to investigate the influence of different tetradecylbenzyltrimethylammonium (BDA-C14) concentrations on inhibitor adsorption morphology and inhibition mechanisms. Analysis of tapping mode topography and phase images on mica show that multiple small holes/defects were present in the uniform inhibitor film at 50 and 100 ppm, which are above the surface saturation concentration. While at 25 ppm (below the surface saturation concentration), a non-uniform inhibitor film with different sizes of holes was detected. At 5 ppm, discontinuous inhibitor aggregates were observed. The contact mode AFM scratching technique was used to obtain the inhibitor film thickness at each concentration, which was consistent with the corresponding depth of holes measured by tapping mode topography. The molecular orientations and inhibitor film structures at each concentration are postulated based on the measured inhibitor film thickness. Observed adsorption morphologies on mica are connected with the corrosion inhibition behavior observed on UNS G1018 steel at each concentration.

**Keywords:** Contact mode AFM, nano-scratching, tapping mode AFM, mica, carbon steel, corrosion inhibitor

## INTRODUCTION

In hydrocarbon production systems, mild steel is overwhelmingly used for the construction of pipelines and tanks for the transmission and storage of crude oil, natural gas, and derived petroleum products. Although mild steel has excellent mechanical properties and low cost, it is susceptible to corrosion attack in typical service environments. Inhibition of internal corrosion is essential for assuring asset integrity of oil and gas transportation pipelines. Corrosion inhibitors are chemical compounds that can significantly, and economically, mitigate corrosion when added continuously in small concentrations.

The adsorption behavior is crucial for the performance of organic inhibitor. The adsorption of organic compounds can be classified as chemical adsorption or physical adsorption. Chemical adsorption forms covalent bonding between the adsorbate and the substrate surface, while physical adsorption depends on the intermolecular interactions between the adsorbate and the substrate surface. The adsorption of surfactants to a metal surface usually belongs to the physical adsorption category, and the intermolecular interactions mainly include electrostatic interactions, dipole-dipole interactions, and dispersion interactions.<sup>1, 2</sup> The driving forces for organic inhibitor adsorption on a metal surface are usually understood to be made up of both electrostatic interactions and hydrophobic interactions.<sup>3</sup> The active components in organic corrosion inhibitors are organic surfactants which are amphiphilic molecules with a polar head group and a long hydrophobic tail. The hydrophilic polar head group physically adsorbs on the surface due to electrostatic interactions. Molecular modelling has indicated that the initial physisorbed inhibitor molecules have random orientations on the substrate surface, either lying down or being tilted. However, due to the hydrophobic interactions between non-polar tails, adsorbed molecules will gradually stand up.<sup>4, 5</sup> After some time, the hydrophobic tails will be oriented perpendicular to the surface and a self-assembled layer formed.<sup>5</sup>

Previous research on corrosion inhibitors mainly focuses on the steel-aqueous solution interfacial electrochemical behavior and corrosion inhibition efficiency.<sup>6-8</sup> However, the inhibitor adsorption behavior and its influence on inhibition performance have rarely gained attention due to the limitation of traditional electrochemical techniques in localized adsorption studies. Atomic force microscopy can be operated *in situ* in liquid environments with a nanometer resolution, which is powerful enough for inhibitor adsorption research. Although most AFM research has been performed with organic surfactant adsorption on various substrates such as mica,<sup>9</sup> graphite, silica,<sup>10</sup> and even gold,<sup>11</sup> there are only a few AFM studies dedicated to corrosion inhibitor research with mild steel.<sup>12-14</sup>

In this present work, tetradecylbenzyltrimethylammonium (BDA-C14) adsorption behavior on mica at various concentrations was investigated by both contact mode and tapping mode AFM, and then the corrosion behavior on mild steel with the same concentrations were analyzed by AFM. Conclusions were drawn based on the consistent observations between adsorption and corrosion behavior.

## EXPERIMENTAL PROCEDURE

### Materials and Solutions

Both mica and steel substrates were used in this current work. Mica substrates were adopted for studying inhibitor adsorption structures and measuring surface coverage considering its atomically flat surface. The steel specimens were machined from UNS G10180 mild steel, and successively polished using 400, 600, 800, and 1200 grit silicon carbide abrasive papers followed by 9, 3, and 1  $\mu\text{m}$  diamond particle loaded paste on a polishing cloth. The samples were then rinsed with ethanol and water and dried in air.

The specific amphiphilic inhibitor model compound used in this work has a polar head group, benzyltrimethylammonium, and a tetradecyl ( $-\text{C}_{14}\text{H}_{29}$ ) hydrophobic tail. Its molecular structure and synthesis reaction are shown in Figure 1, and the detailed synthesis and characterization are described

© 2023 Association for Materials Protection and Performance (AMPP). All rights reserved. No part of this publication may be reproduced, stored in a retrieval system, or transmitted, in any form or by any means (electronic, mechanical, photocopying, recording, or otherwise) without the prior written permission of AMPP.

Positions and opinions advanced in this work are those of the author(s) and not necessarily those of AMPP. Responsibility for the content of the work lies solely with the author(s).

in a previous publication.<sup>15</sup> The shortened name for this structure is BDA-C14, corresponding to tetradecylbenzyl-dimethylammonium, used in the form of its bromide salt.

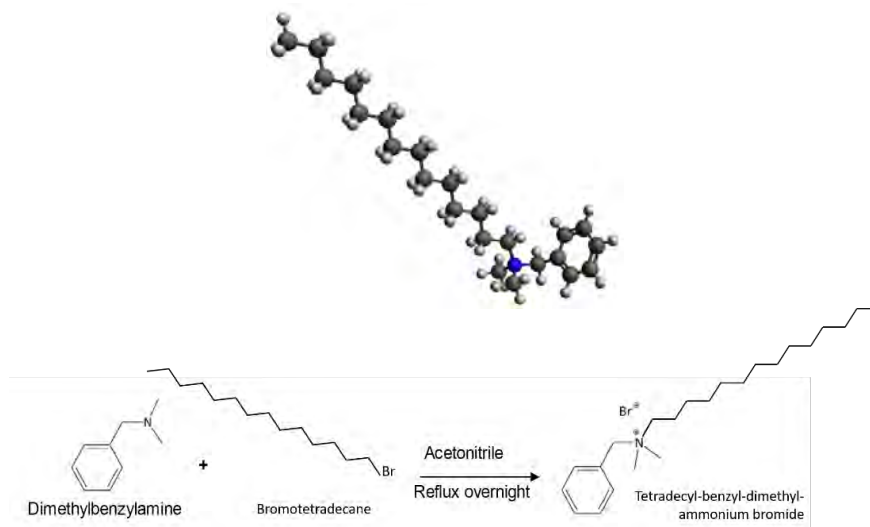


**Figure 1: Molecular structure and synthesis reaction of tetradecylbenzyl-dimethylammonium (BDA-C14)**

In order to complete a systematic study, the inhibitor adsorption behavior on mica has been investigated at multiple inhibitor concentrations. The inhibitor behavior at the concentration above surface saturation (100 ppm) has been reported in a previous publication in order to study the inhibitor adsorption behavior at a saturation coverage condition.<sup>4</sup> The surface saturation concentration was determined in our previous electrochemistry work<sup>16</sup> as well as in the AFM work.<sup>15, 17</sup> In the results presented below, the adsorption behavior was studied at surface saturation concentration (50 ppm), at a concentration below the surface saturation (25 ppm), and at a very low concentration (5 ppm). All solutions were prepared using deionized water with a conductivity of 18 MΩ cm<sup>-1</sup>. The experimental matrix is shown in Table 1.

**Table 1**  
**Experimental matrix for effect of inhibitor concentration on adsorption behavior studies.**

<b>Temperature</b>	Room temperature 25°C
<b>Material</b>	Mica, UNS G1018
<b>Inhibitor concentration</b>	Blank solution (0 ppm), 5 ppm, 25 ppm, 50 ppm, 100 ppm
<b>NaCl concentration</b>	1 wt. %
<b>Atmosphere</b>	CO <sub>2</sub>
<b>pH</b>	Initial 3.9 ± 0.1
<b>Flow rate</b>	0 m/s
<b>Sample area</b>	1.2 cm <sup>2</sup>
<b>EC-AFM cell</b>	3 mL
<b>Technique</b>	<i>In situ</i> contact mode nano-scratching, tapping mode AFM topography and phase imaging

## ***In situ* Contact Mode and Tapping Mode AFM Measurements**

A commercial Molecular Imaging<sup>†</sup> and a commercial Keysight<sup>‡</sup> Scanning Probe Microscope system equipped with a fluid cell attachment were used in the research reported in this paper. Triangular silicon cantilevers with a nominal spring constant of 0.38 N/m were adopted for both contact mode and tapping mode operation modes. Measurements were made at the mica-aqueous solution interface in order to analyze the inhibitor film structure. The scan rate of the AFM probe was set to 1000 nm/s for a 1 × 1 μm<sup>2</sup> scan area on mica. A resolution of 512 by 512 pixels was adopted for all AFM images.

A contact mode AFM nano-scratching technique was adopted in this current work in order to investigate the exact layer structure and measure film thickness at various inhibitor concentrations. The nano-scratching procedure has been described in detail in a previous publication.<sup>12</sup>

In order to minimize the lateral force and retain the original inhibitor film topography, tapping mode AFM was adopted. For tapping mode, topography images as well as phase images were obtained. The resonance frequency, which is usually around 25 kHz in liquid, would be tuned before each experiment. The drive frequency was set as 0.1 kHz less than the resonance frequency.<sup>18</sup> The setpoint amplitude was between 1.0 V and 1.2 V. The phase image records the phase lag of cantilever oscillation when the tip contacts a surface with different stiffness or hardness properties.<sup>19, 20</sup> In this work, tapping mode phase imaging was used for distinguishing soft inhibitor film and hard mica substrate surfaces.

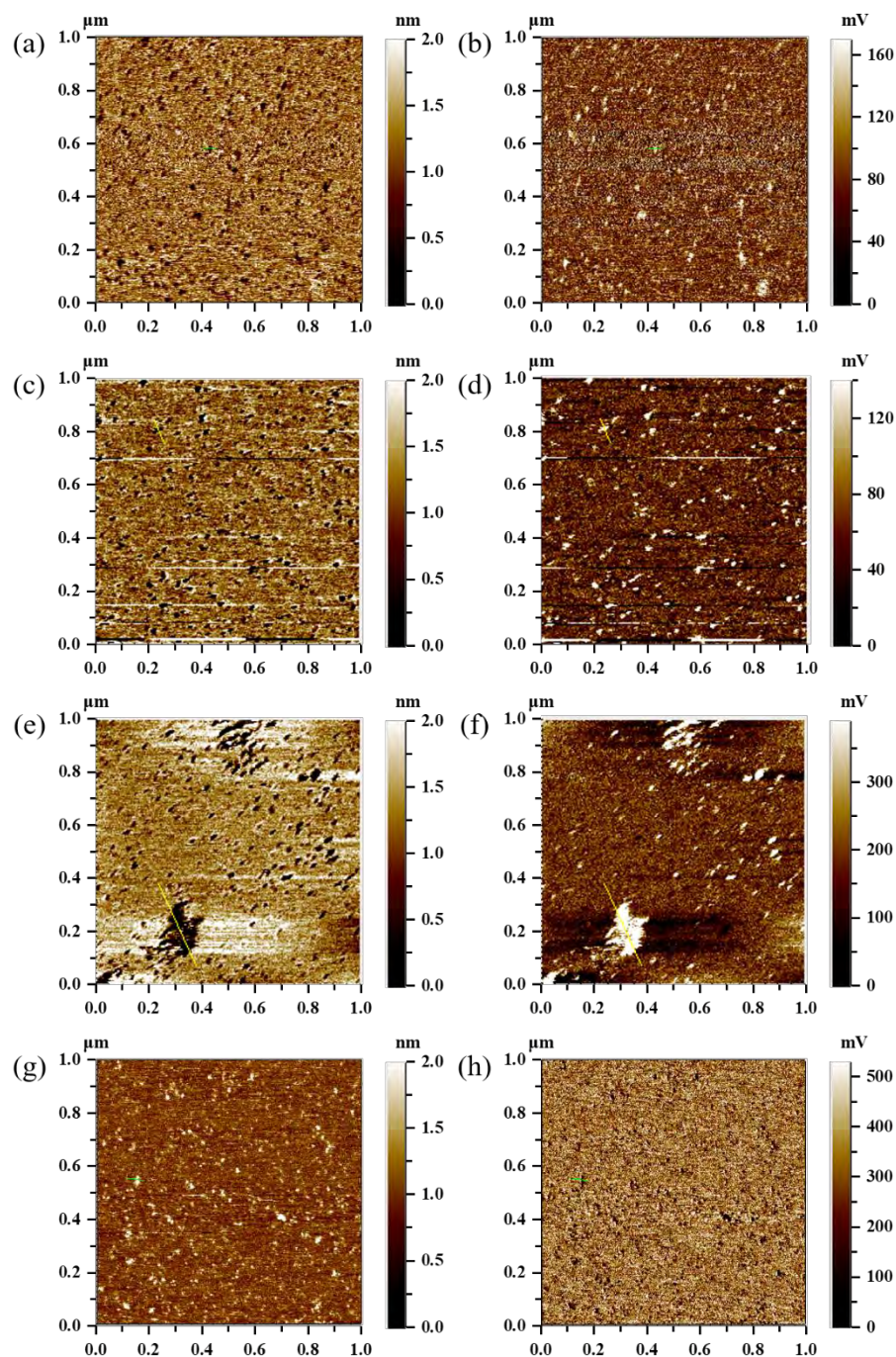
## **RESULTS**

Figure 2 shows tapping mode AFM images of the inhibitor film on mica at various concentrations from 5 to 100 ppm. Figure 2a shows the adsorption behavior of BDA-C14 on mica at 100ppm. The topography is a map of surface height, while the phase image indicates the relative surface hardness or softness of the measured surface. As shown in the tapping mode topography image (Figure 2a), the surface is uniform at this concentration, although multiple small defects are observed on the inhibitor film. This topography image shows that “black holes” are observed, which indicates numerous small open areas in the corrosion inhibitor layer. In the corresponding locations of phase images (Figure 2b), bright spots are observed, indicating in these “black hole” locations the surface is harder (being mica) than on the surrounding surface (being the soft inhibitor film). This confirms the locations of the holes are indeed the mica surface with a relatively larger hardness. At 50 ppm (Figure 2c and Figure 2d), the surface morphology looks similar to 100ppm; it is a uniform film with multiple small defects. At 25 ppm (Figure 2e and Figure 2f), the adsorption morphology is a little different from that at higher concentrations. The topography image shows the surface as non-uniform with different types of holes observed. Small holes similar to those observed for 50 and 100 ppm are found, but there are also big clusters of holes at 25ppm. Repeated results show that the inhibitor film is non-uniform at 25 ppm. At 5 ppm (Figure 2g and Figure 2h), the inhibitor adsorption morphology is quite different from the other three higher concentrations. Multiple bright spots are observed in the topography image, indicating these locations are higher than the surrounding regions while the phase image indicates these higher locations are softer than the surrounding regions. This confirms multiple small, adsorbed inhibitor aggregates. These discontinuous inhibitor aggregates indicate that there is no continuous film formation at 5 ppm concentration, which is a big difference compared with the other concentrations. In the following section, detailed analysis of inhibitor film thickness and postulated molecular orientations are provided for each concentration.

---

<sup>†</sup> Trade Name

<sup>‡</sup> Trade Name



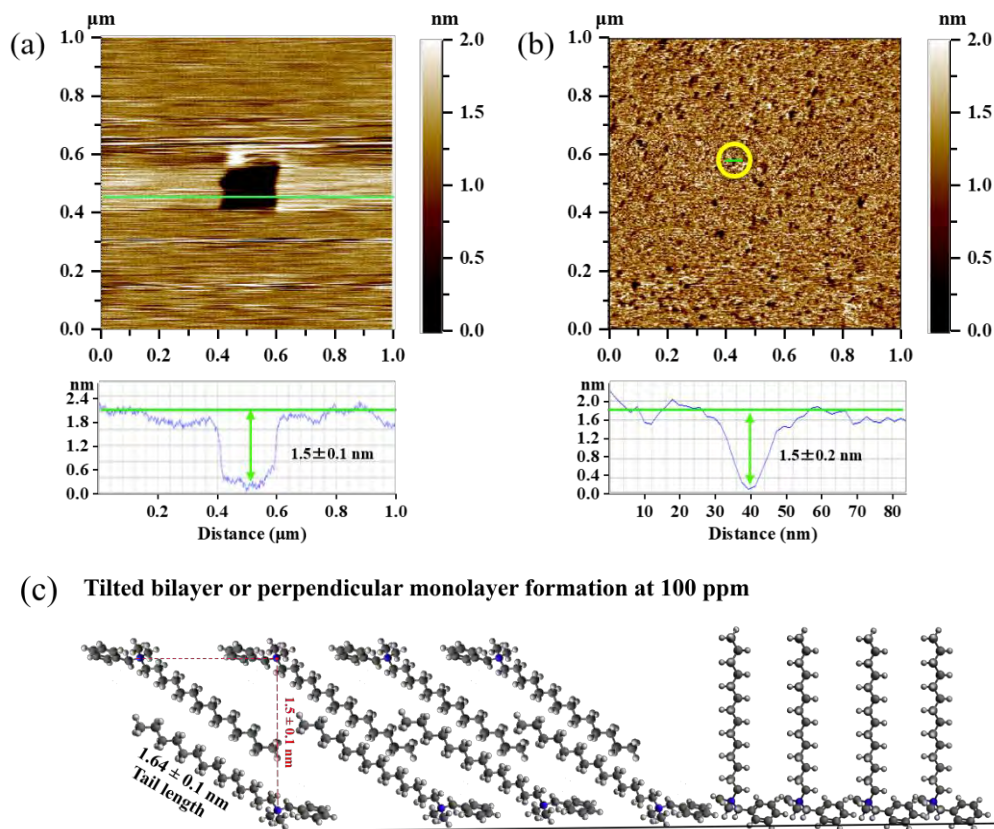
**Figure 2: Tapping mode AFM images of inhibitor film formed on mica at various concentrations of BDA-C14 in 1 wt.% NaCl: (a) topography image-100 ppm; (b) phase image-100 ppm; (c) topography image-50 ppm; (d) phase image-50ppm; (e) topography image-25 ppm; (f) phase image-25 ppm; (g) topography image-5 ppm; (h) phase image-5 ppm.**

### **Study of inhibitor adsorption on mica at 100 and 50 ppm with contact mode and tapping mode AFM**

Figure 3 shows the contact mode nano-scratching and tapping mode imaging results at 100 ppm. In order to further investigate the structure of the adsorbed layers, the thickness of the adsorbed layer for 100 ppm inhibitor concentration was measured by performing both contact mode AFM nano-scratching tests (Figure 3a) and tapping mode imaging (Figure 3b).

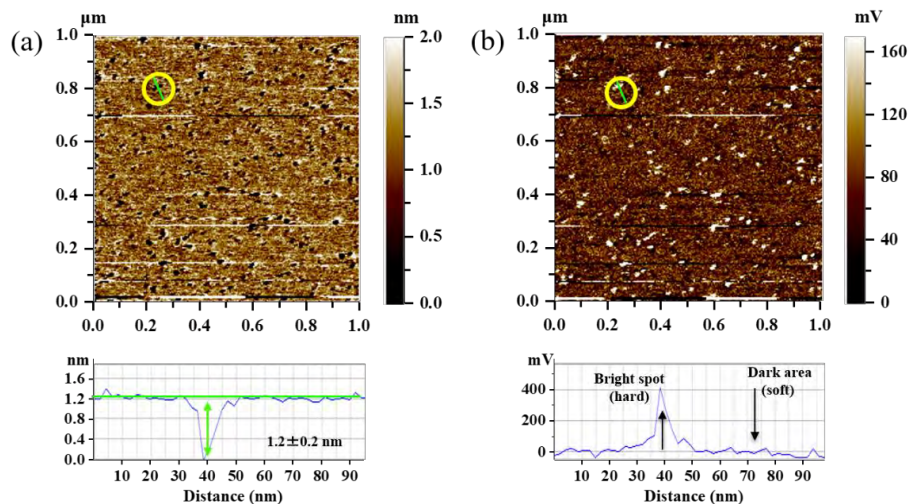
Contact mode AFM nano-scratching was performed at this 100ppm concentration to measure the film thickness, as shown in Figure 3c. The strategy was to scratch away a small area of inhibitor film with a higher force, and then measure the height difference between the scratched area and the surrounding area. The film thickness was measured to be around 1.5 nm, which is consistent with the depth of the holes measured in tapping mode (Figure 3a). The inhibitor film thickness in this location can be estimated as also around  $1.5 \pm 0.2$  nm from the tapping mode topography image (Figure 3b) by measuring the depth of the detected holes.

Comparing the inhibitor film thickness with the molecular tail length (1.64 nm), the inhibitor film thickness is slightly smaller than the molecular tail length. Therefore, it is proposed that at this condition with 100 ppm BDA-C14, the inhibitor molecules either forms a tilted bilayer or forms a vertical monolayer (Figure 3c). This postulation has been discussed in detail in a previous publication.<sup>15</sup>



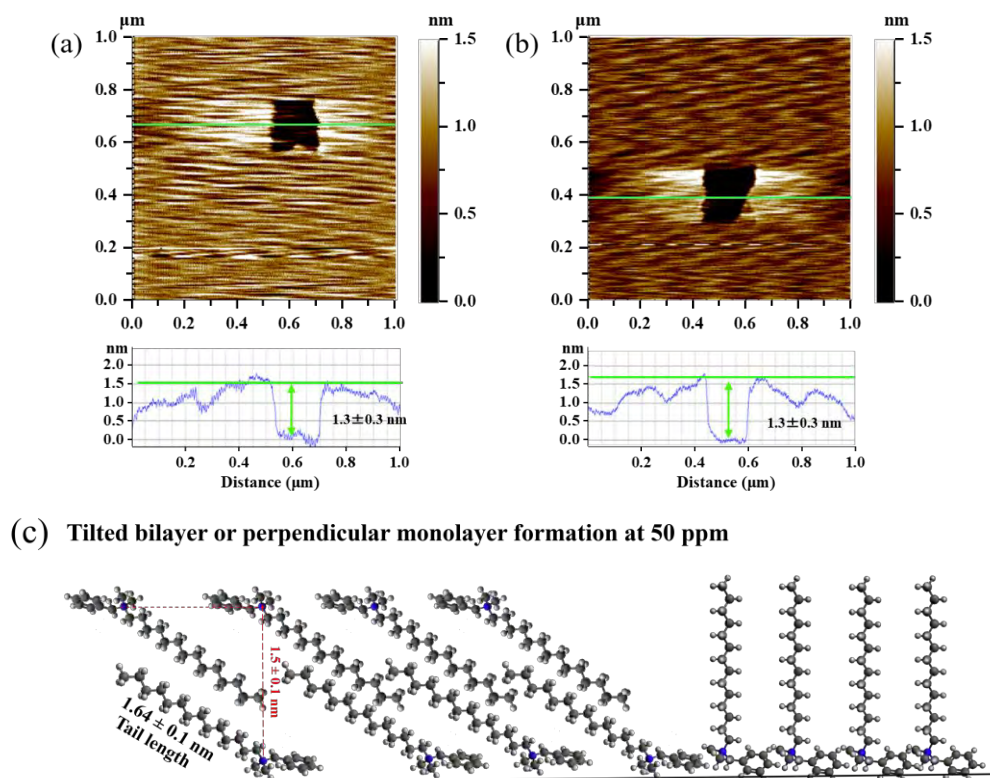
**Figure 3: Topography images at 100 ppm BDA-C14 on mica: (a) obtained after contact mode nano-scratching; (b) tapping mode. Schematic (c) shows likely molecular orientation for a tilted bilayer or perpendicular monolayer. (The layer thickness was determined by measuring the height difference between scratched and unscratched areas on a height profile. Height profiles were plotted along the green line appearing in the corresponding topography image).**

At 50ppm concentration, the topography (Figure 4a) shows multiple holes/lower spots, while the phase image (Figure 4b) shows brighter spots in the corresponding hole locations, indicating these hole locations are harder than surrounding soft inhibitor film. Therefore, it can be concluded from the topography and phase image that multiple defects exist in the inhibitor film. The average depth of holes was measured to be around  $1.2 \pm 0.2$  nm.



**Figure 4: Tapping mode AFM image of inhibitor film formed on mica for 50 ppm BDA-C14 in 1 wt.% NaCl: (a) topography image and cross-section profile of a hole; (b) phase image and cross-section profile of a bright spot.**

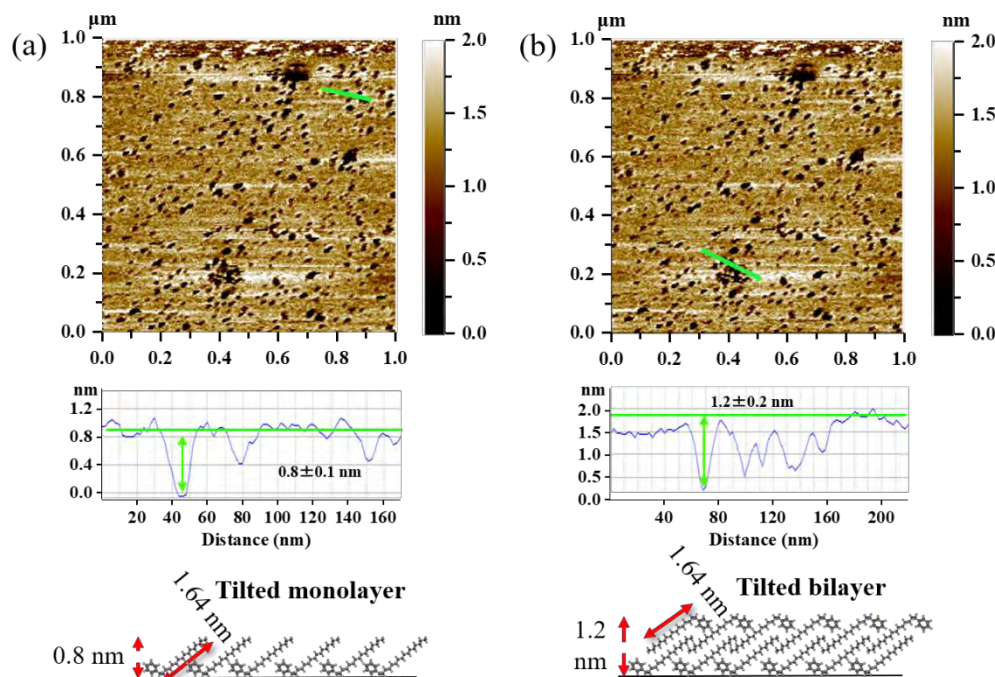
Contact mode scratching tests have been performed for this 50 ppm concentration. Figure 5a and b show the topography images after scratching on two different samples. The average scratch depth is around 1.3 nm. This is consistent with tapping mode results. When comparing the film thickness with the molecular tail length, the molecular structure could be proposed as a tilted bilayer or a less tilted monolayer (Figure 5c).



**Figure 5: Contact mode nano-scratching topography images with different mica samples at 50ppm: (a) sample I; (b) sample II; (c) schematic diagram of possible BDA-C14 inhibitor molecular orientations.**

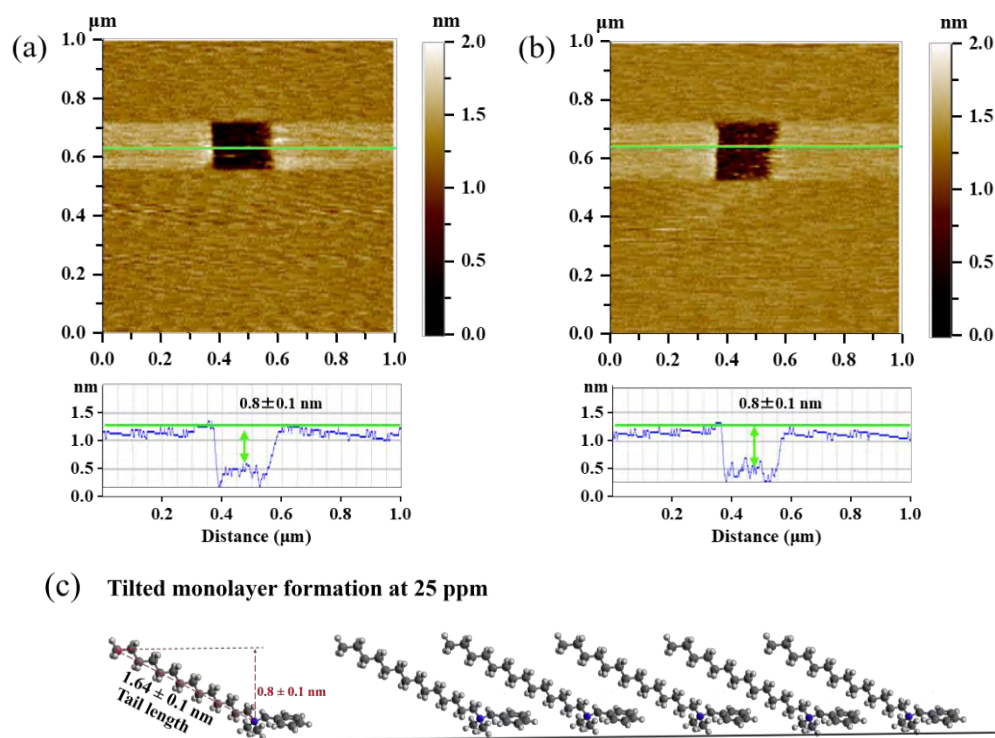
## Study of inhibitor adsorption on mica at 25 ppm with contact mode and tapping mode AFM

Figure 6 displays the topography and phase images at 25 ppm. A non-uniform inhibitor film with different types of holes were detected by the topography image (Figure 6a). Both small holes and big clusters of holes were observed. From the phase images (Figure 6b), it can be seen that both types of hole location show brighter contrast than surrounding inhibitor film, indicating a harder mica surface was exposed in these locations. By measuring the depth of these holes, it has been found that the small holes have an average depth of 0.8 nm, while these large cluster of holes have an average depth of 1.2 nm. This means that during the formation of the large clusters of holes, the surrounding inhibitor film surface seems to be elevated. This can be caused by the change of inhibitor molecular orientation. Also, the film thickness surrounding these large holes is similar to the film thickness at higher concentration (50 ppm BDA-C14 in Figure 5), probably indicating that during the clustering process, inhibitor molecules surrounding these large holes evolve to similar structures as at 50 ppm.



**Figure 6: Tapping mode AFM image of inhibitor film formed on mica for 25 ppm BDA-C14 in 1 wt.% NaCl: (a) topography image, cross-section in small holes location and proposed molecular orientation; (b) topography image, cross-section in large cluster of holes location and proposed molecular orientation.**

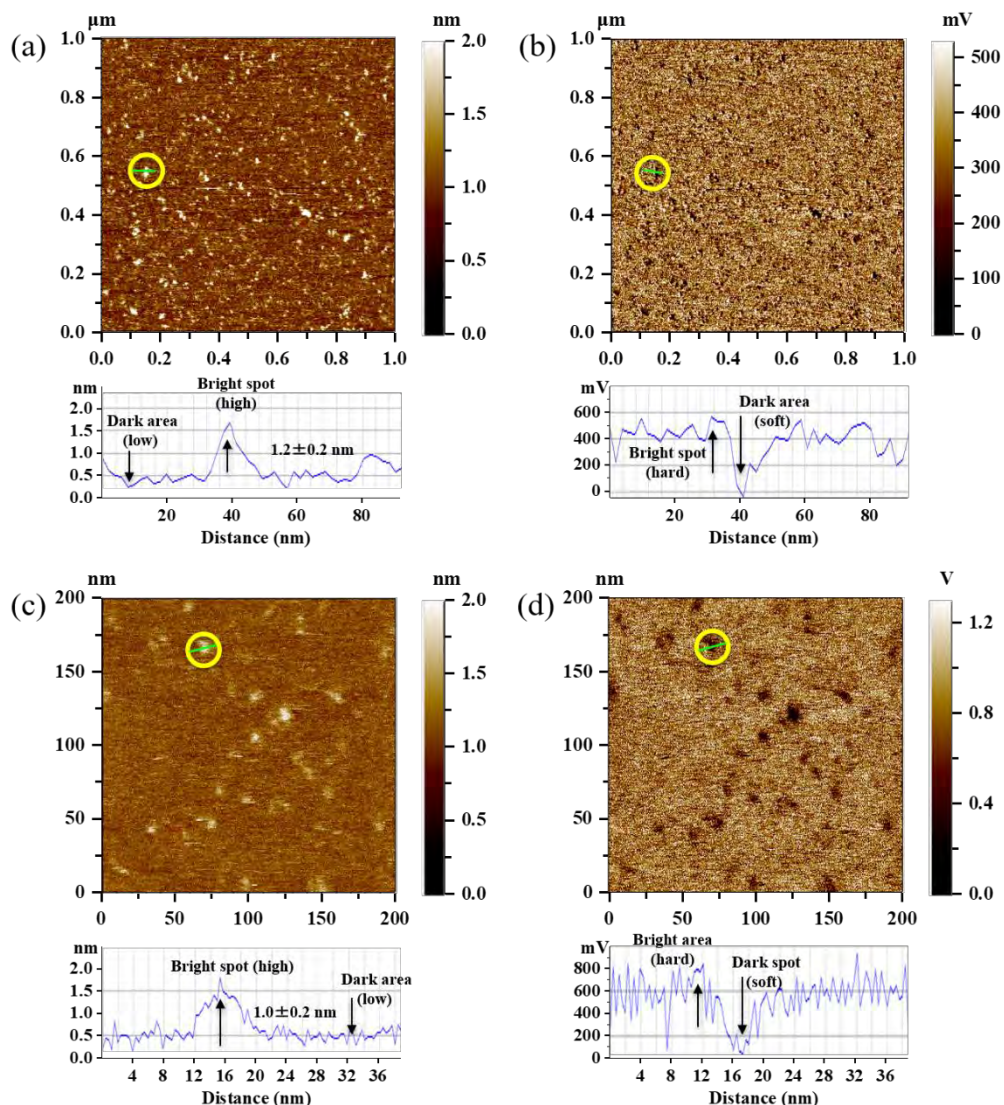
Figure 7a and 7b shows the contact mode images after scratching at 25ppm concentration of BDA-C14. By measuring the scratching depth, the inhibitor film thickness is determined to be around 0.8nm. Comparing the film thickness with the molecular tail length (1.64nm), the molecular structure could be a tilted monolayer as shown in Figure 7c.



**Figure 7: Contact mode nano-scratching AFM image of inhibitor film formed on mica for 25 ppm BDA-C14 in 1 wt.% NaCl solution, after scratching topography: (a) sample I; (b) sample II; (c) schematic diagram of possible BDA-C14 inhibitor molecular orientations.**

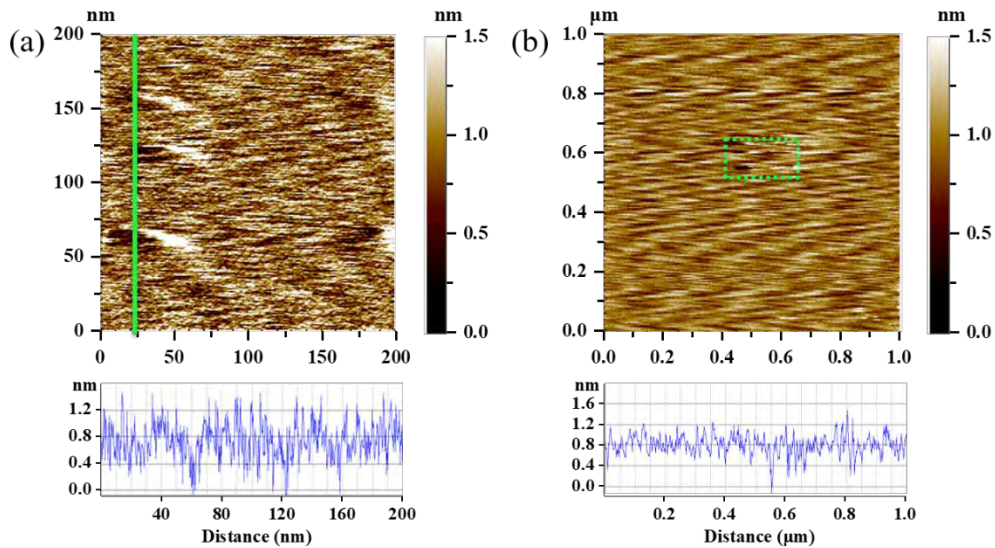
### Study of inhibitor adsorption on mica at 5 ppm with contact mode and tapping mode AFM

Figure 8 shows tapping mode images of inhibitor adsorption on mica at 5 ppm with two different scan sizes (1  $\mu\text{m}$  and 200 nm). The topography (Figure 8a) shows multiple higher spots, while the phase image (Figure 8b) indicates these higher spots are darker than the surrounding area. This indicates these higher spots are softer than the surrounding mica surface; therefore, it can be inferred that these spots are actually inhibitor aggregates. Figure 8c shows a zoomed in topography image. It can be seen more clearly that there are multiple higher spots. The corresponding phase image further confirms that these are inhibitor aggregates because these spots are darker and softer than the surrounding mica surface.



**Figure 8: Tapping mode AFM image of inhibitor film formed on mica for 5 ppm BDA-C14 in 1 wt.% NaCl solution: (a) topography image with  $1 \times 1 \mu\text{m}^2$  scan size; (b) phase image with  $1 \times 1 \mu\text{m}^2$  scan size; (c) topography image with  $200 \times 200 \text{nm}^2$  scan size; (d) phase image with  $200 \times 200 \text{nm}^2$  scan size.**

The tapping mode results have shown that at 5 ppm there are discontinuously distributed inhibitor aggregates. In order to further investigate the film formation at 5 ppm, contact mode scratching was also performed at the same condition. Figure 9a is a 200 nm small area captured during scratching. Figure 9b is a larger area captured after scratching. As can be seen there is no visible scratched square in Figure 9b, indicating there was no continuous film that could be scratched away. This further verified that at 5 ppm, there was no continuous film formation and there were only inhibitor aggregates formed on the mica surface.



**Figure 9: Contact mode AFM image of inhibitor film formed on mica for 5 ppm BDA-C14 in 1 wt% NaCl: (a) topography image during scratching -  $200 \times 200 \text{ nm}^2$ ; (b) topography image after scratching -  $1 \times 1 \text{ }\mu\text{m}^2$ .**

In summary, Figure 10 lists the measured inhibitor film thicknesses by contact mode scratching and tapping mode holes depth, respectively, at the three BDA-C14 tested concentrations. At 100 ppm and 50 ppm, it can be seen the inhibitor film thickness measured by these three methods are comparable and mostly are between 1.2 to 1.5 nm. At 25 ppm, the contact mode AFM measured thickness is around 0.8 nm, which is consistent with the depth of small holes at 25 ppm. While at 5 ppm, there was no scratched square after contact mode scratching and, therefore, is not shown on the Figure 10, indicating there was no continuous inhibitor film. This is consistent with the discontinuous inhibitor aggregates observed by tapping mode at 5 ppm. Inhibitor film thicknesses of BDA-C14 measured by QCM<sup>21</sup> is also consistent with the film thickness measured by two AFM operation modes here.

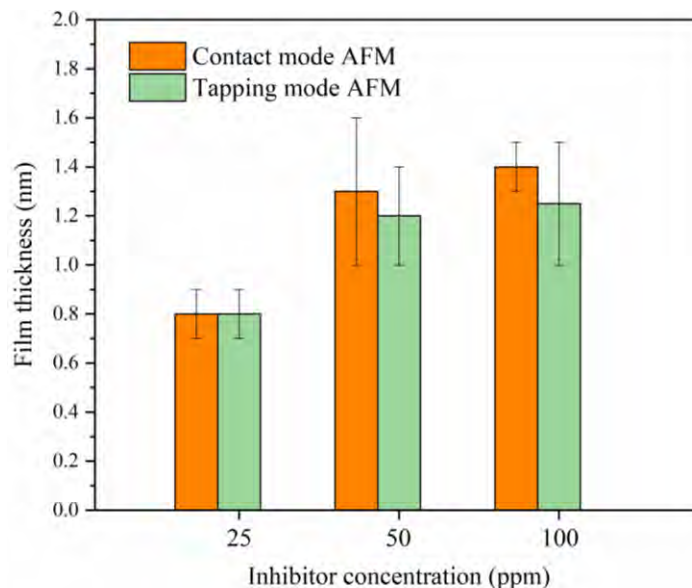


**Figure 10: Summary of film thickness measured by three different techniques: contact mode AFM and tapping mode AFM on mica.**

## Connection between inhibitor adsorption on mica and corrosion inhibition mechanisms on UNS G1018 steel at various concentrations

In the previous discussion, the inhibitor adsorption behavior on mica has been analyzed at different concentrations through the AFM contact mode and tapping mode. The corrosion inhibition behaviors at the same concentrations are discussed below.

The adsorption behavior on mica and the corrosion inhibition behavior on UNS G1018 steel at 100 and 50 ppm are compared. The adsorption morphology (Figure 3b and Figure 4) on mica shows a uniform inhibitor film with evenly distributed small defects formed. As for the UNS G1018 steel, it can be seen that the whole surface was uniformly protected (Figure 11). Ten minutes after adding the inhibitor, its molecules readily adsorbed as indicated by the fact that there is no continuous observable corrosion from 10 minutes to 4 hours for both 100 ppm (Figure 11 a and b) and 50 ppm (Figure 11 c and d) BDA-C14. This protection phenomenon is consistent with the uniform inhibitor film on mica at 100 ppm and 50 ppm.

Moreover, simultaneous LPR corrosion rates of 1018 steel in BDA-C14 solutions in our previous work<sup>15, 17</sup> show that the steady state corrosion rates increase with concentration, while at 50 and 100 ppm the steady state corrosion rates are similar and stabilize at a similarly low value, indicating surface saturation concentration has been reached and surface saturation inhibition efficiency has been reached at both concentrations. However, one can find that at these two saturated concentrations, the corrosion rate is still not zero and the inhibition efficiency is not 100%. This phenomenon has been observed extensively for various surfactant types of inhibitor.<sup>22-24</sup> This could be related to the small and evenly distributed defects in the inhibitor film that were observed on mica.

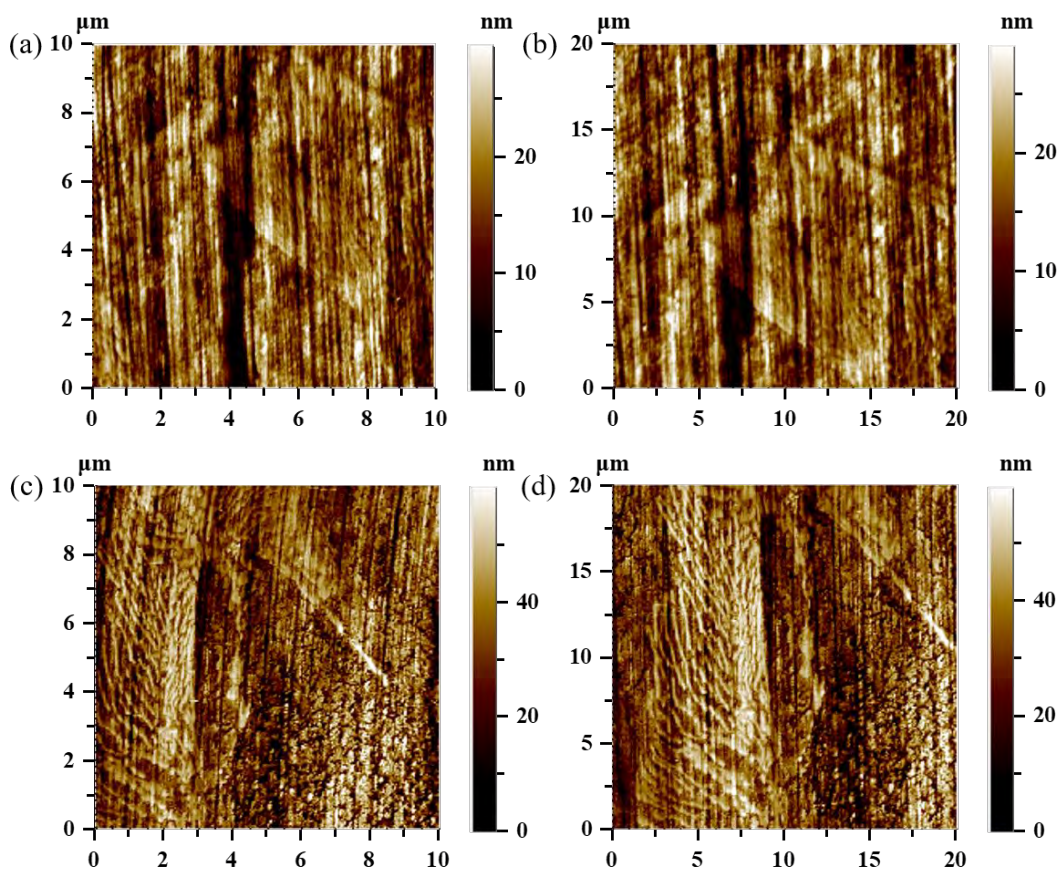


**Figure 11: Topography AFM images of UNS G1018 steel in BDA-C14 at saturated concentration 100 and 50 ppm with different immersion time: (a) 100 ppm, 10 minutes; (b) 100 ppm, 4 hours; (c) 50 ppm, 10 minutes; (d) 50 ppm, 4 hours. Experimental conditions: 25°C, initial pH 3.9. CO<sub>2</sub> saturated 1 wt.% NaCl aqueous solution.**

The comparison between the adsorption behavior on mica and the corrosion inhibition behavior on UNS G1018 steel have also been made at 25ppm. As discussed in a previous section with a mica surface, inhibitor molecules form a non-uniform film at 25ppm (Figure 6). There are two types of holes observed: small holes and big clusters of holes. This is different from the uniform small holes at 50 ppm and 100 ppm and is expected to be different for a mild steel surface. As for 1018 steel, the results at 25 ppm have been shown in Figure 12. Two different levels of protection are observed. Some regions of the surface are protected similar as in experiments with higher concentrations (100 ppm and 50 ppm), where there was no continuous observable corrosion as immersion time increased from 10 minutes (Figure 12a) to 4 hours (Figure 12b). However, in other regions of the same sample, the surface corroded as if it was uninhibited with surface variations between iron carbide and ferrous iron regions of 300 nm in 4 hours, corresponding to 0.7 mm/yr (Figure 12d). These regions with continuous corrosion could be related to the large cluster of defects on the inhibitor film found on mica. The large clusters of defects could be where corrosion initiated and proceeded.

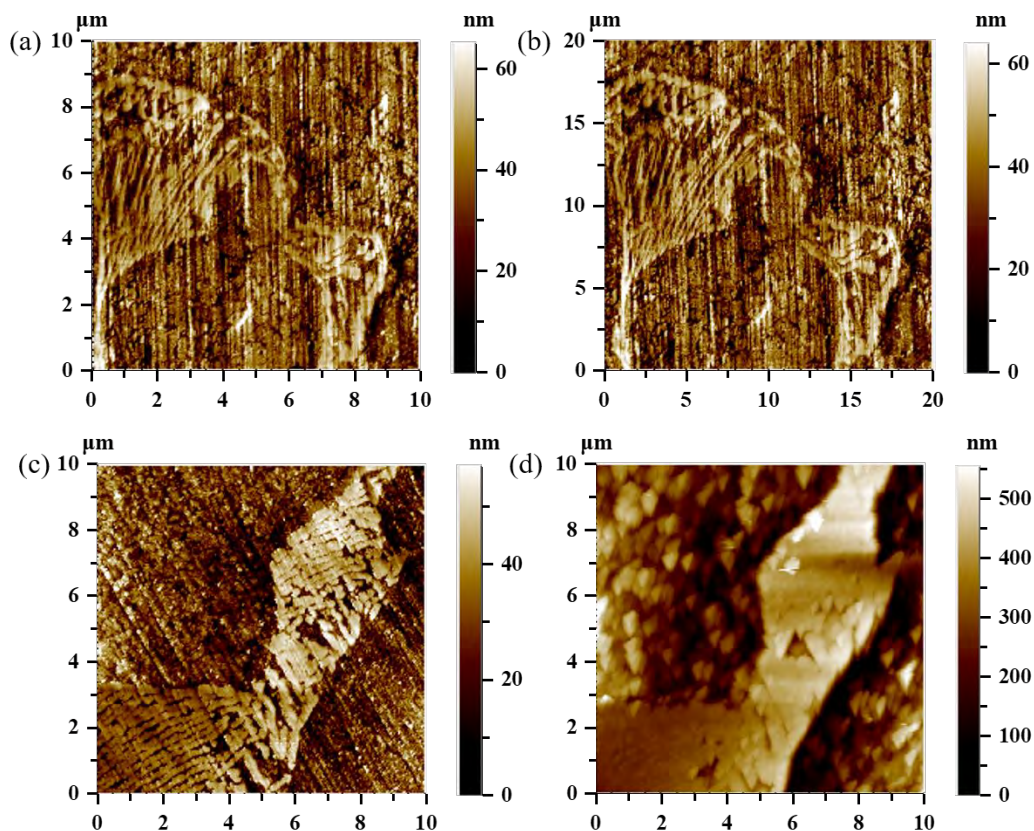


**Figure 12: Topography AFM images of UNS G1018 steel in BDA-C14 at non-saturated concentration 25 ppm with different immersion time: (a) protected region, 10 minutes; (b) protected region, 4 hours; (c) non-protected region, 10 minutes; (d) non-protected region, 4 hours. Experimental conditions: 25°C, initial pH 3.9. CO<sub>2</sub> saturated 1 wt.% NaCl aqueous solution.**

At 5 ppm, on a mica surface there is no continuous inhibitor film formation, and only discontinuous inhibitor aggregates are observed (Figure 8). On a 1018 steel surface, Figure 13 shows a real-time monitoring of the 1018 steel surface topography evolution at 5 ppm to provide detailed information about

how the surface corrosion evolved at this low inhibitor concentration. The evolution of a fixed location at 5 ppm was captured continuously from 5 minutes to 1 hour. The height difference between cementite and ferrite corresponding to each immersion time is listed in the Figure 13 caption. From Figure 13 a to f, the height difference between cementite and ferrite gradually increases with immersion time. The ferrite gradually dissolved while the cementite remained intact. At this 5 ppm BDA-C14 value, the whole surface corroded uniformly as this location in Figure 13 as detected by multiple measurements.

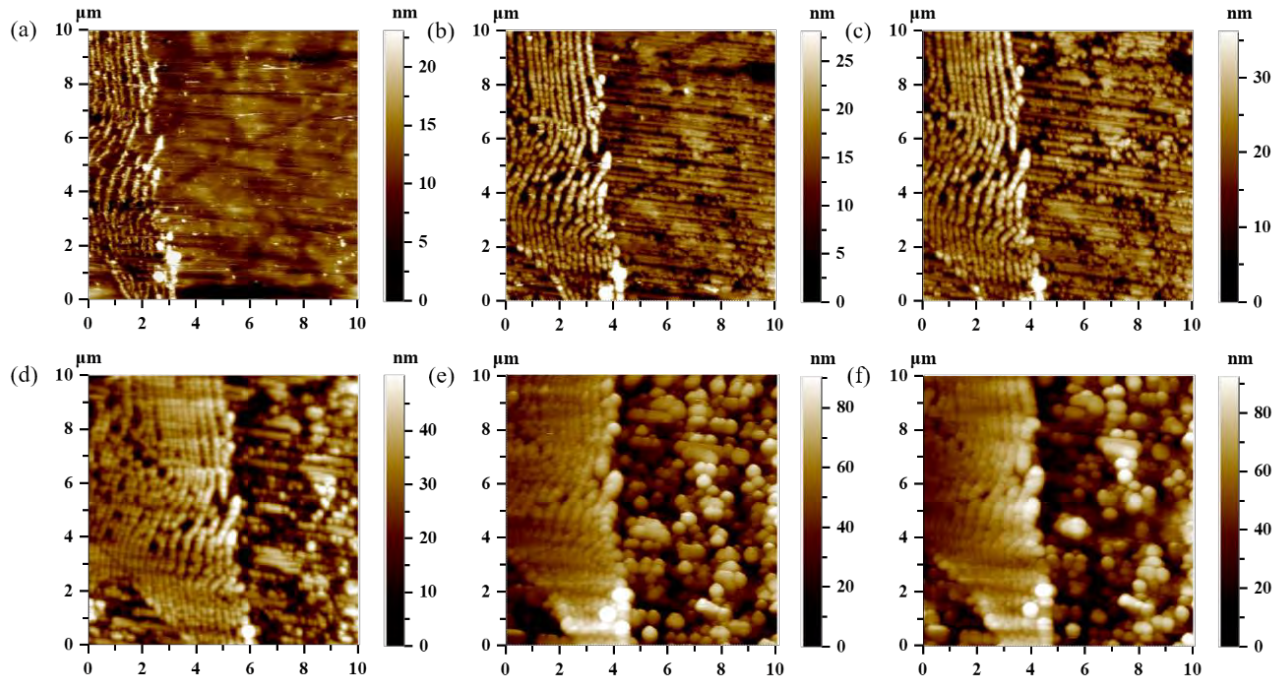


**Figure 13: Real time AFM topography images for monitoring the surface corrosion evolution: (a) immersion 4 minutes, height difference < 10 nm; (b) immersion 7 minutes, height difference < 10 nm; (c) immersion 10 minutes, height difference ~15 nm; (d) immersion 17 minutes, height difference ~40 nm; (e) immersion 39 minutes, height difference ~50 nm; (f) immersion 1 hour, height difference ~70 nm. Experimental conditions: 25°C, initial pH 3.9. CO<sub>2</sub> saturated 1 wt.% NaCl aqueous solution.**

Figure 14 shows the comparison of 1018 steel corroded surface topography in blank solution and in 5 ppm BDA-C14 solution. Figure 14a, b, and c display the topography images of steel surface in 5 ppm inhibitor solution and reveal a corrosion behavior similar to that observed in an aqueous solution in the absence of inhibitor (see Figure 11d, e, and f). Based on the surface topography profiles in Figure 11a, b, and c, the height differences between the cementite structure and surrounding ferrite are measured as  $10 \pm 5$  nm,  $70 \pm 20$  nm, and  $200 \pm 40$  nm after exposure in the 5 ppm BDA-C14 inhibitor solution for 10 minutes, 1 hour and 4 hours, respectively. It is determined from these height difference values, utilizing (1), that the corrosion rate between 10 minutes to 1 hour is  $0.63 \pm 0.2$  mm/year and the time averaged local corrosion rate from 1 hour to 4 hours exposure is estimated as  $0.38 \pm 0.3$  mm/year, which are of the same magnitude as (even if the average is a little lower than) those estimated for an inhibitor-free solution ( $0.74 \pm 0.2$  mm/year from 10 mins to 1 hour and  $0.5 \pm 0.2$  mm/year from 1 hour to 4 hours as reported in previous work.<sup>15</sup> Therefore, it can be deduced that at 5 ppm the surface is not protected well and uniform corrosion still proceeds with a similar or slightly slower rate as in blank solution, indicating the corrosion rate at 5 ppm is only slightly reduced by the inhibitor.

$$\text{corrosion rate} = \frac{70 \text{ nm} \pm 20 - 200 \text{ nm} \pm 40}{50} \text{ mins} * 60 \left( \frac{\text{min}}{\text{hr}} \right) * 24 \left( \frac{\text{hr}}{\text{day}} \right) * \frac{365 \left( \frac{\text{day}}{\text{year}} \right)}{10^6 \left( \frac{\text{nm}}{\text{mm}} \right)} = 0.63 \pm 0.2 \text{ mm/year} \quad (1)$$

In summary, at 5 ppm the whole surface uniformly corroded and there was no well protected area as at higher BDA-C14 concentrations. This could be related to the fact that no continuous inhibitor film formation was observed at 5 ppm with the mica tests where there were only discontinuous inhibitor aggregates, which did not provide good inhibition.

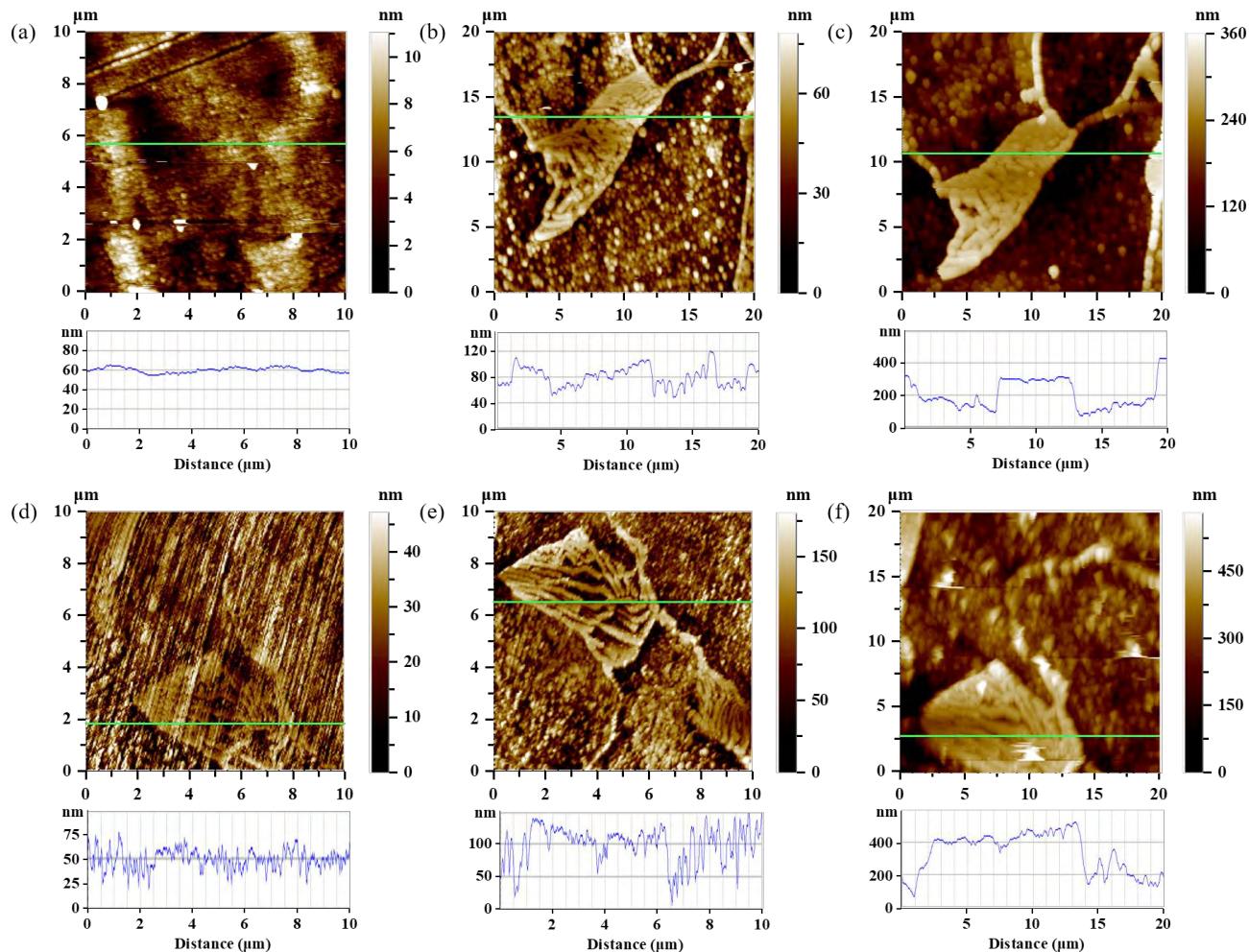


**Figure 14: Topography AFM images of UNS G1018 steel in 5 ppm BDA-C14 and blank solution with different immersion time: 5 ppm (a), 10 minutes; (b) 1 hour; (c) 4 hour; Blank (d), 10 minutes; (e) 1 hour; (f) 4 hour. Experimental conditions: 25 °C, initial pH 3.9. CO<sub>2</sub> saturated 1 wt.% NaCl aqueous solution.**

## CONCLUSIONS

Based on contact mode and tapping mode AFM imaging results and proposed adsorption mechanism, these conclusions were drawn:

- At 100 ppm and 50 ppm BDA-C14: uniform film with evenly distributed small defects forms on mica; uniform protection of steel surface whereas an extremely low corrosion rate (but not zero) occurs on carbon steel (UNS G1018).
- 25 ppm BDA-C14: non-uniform film with two different types of holes: small holes and big clusters of holes forms on mica whereas partial corrosion mitigation occurs on the carbon steel surface.
- 5 ppm BDA-C14: discontinuous inhibitor aggregates form on mica and there is no continuous inhibitor film whereas uniform corrosion occurs on carbon steel with corrosion rate slightly lower than in the blank solution.

## ACKNOWLEDGEMENTS

The author would like to thank the following companies for their financial support:

Ansys, Baker Hughes, Chevron Energy Technology, Clariant Corporation, ConocoPhillips, ExxonMobil, M-I SWACO (Schlumberger), Multi-Chem (Halliburton), Occidental Oil Company, Pertamina, Saudi Aramco, Shell Global Solutions and TotalEnergies. This work is partially supported by National Science Foundation CBET Grant 1705817. Dr David Young is also thanked for synthesizing the BDA-C14 used in this work, as well as for assistance in preparing this paper.

## REFERENCES

1. T. Roques-Carmes, S. Aouadj, C. Filiâtre, F. Membrey, A. Foissy, "Interaction between poly (vinylimidazole) and sodium dodecyl sulfate: Binding and adsorption properties at the silica/water interface," *Journal of Colloid and Interface Science* 274 (2004): pp. 421-432.
2. G.Y. Elewady, I.A. El-Said, A.S. Fouda, "Anion surfactants as corrosion inhibitors for aluminum dissolution in HCl solutions," *International Journal of Electrochemical Science* 3 (2008): pp. 177-190.
3. M.A. Migahed, M. Abd-El-Raouf, A.M. Al-Sabagh, H.M. Abd-El-Bary, "Effectiveness of some non ionic surfactants as corrosion inhibitors for carbon steel pipelines in oil fields, " *Electrochimica Acta* 50 (2005) : pp. 4683-4689.
4. H. Wang, B. Brown, A. Pailleret, S. Nestic, "Investigation of inhibitor adsorption mechanism by in situ tapping mode atomic force microscopy, " *CORROSION 2021*, paper no.16610 (Virtual Conference: AMPP 2021).
5. X. Ko, S. Sharma, "Adsorption and Self-Assembly of Surfactants on Metal–Water Interfaces," *The Journal of Physical Chemistry B* 121 (2017): pp. 10364-10370.
6. W. Lorenz, F. Mansfeld, "Interface and interphase corrosion inhibition," *Electrochimica Acta* 31 (1986) : pp. 467-476.
7. C. Cao, "On electrochemical techniques for interface inhibitor research," *Corrosion Science* 38 (1996) : pp. 2073-2082.
8. Y.J. Tan, S. Bailey, B. Kinsella, "An investigation of the formation and destruction of corrosion inhibitor films using electrochemical impedance spectroscopy (EIS)," *Corrosion Science* 38 (1996): pp. 1545-1561.
9. S. Manne, J.P. Cleveland, H.E. Gaub, G.D. Stucky, P.K. Hansma, "Direct visualization of surfactant hemimicelles by force microscopy of the electrical double layer," *Langmuir* 10 (1994): pp. 4409-4413.
10. S. Manne, H.E. Gaub, "Molecular organization of surfactants at solid-liquid interfaces," *Science* 270 (1995): pp. 1480-1482.
11. M. Jaschke, H.J. Butt, H.E. Gaub, S. Manne, "Surfactant Aggregates at a Metal Surface," *Langmuir* 13 (1997): pp. 1381-1384.

12. Y. Xiong, B. Brown, B. Kinsella, S. Nestic, A. Pailleret, "Atomic force microscopy study of the adsorption of surfactant corrosion inhibitor films," *Corrosion* 70 (2014): pp. 247-260.
13. V. Pandarinathan, K. Lepkova, S.I. Bailey, T. Becker, R. Gubner, "Adsorption of corrosion inhibitor 1-dodecylpyridinium chloride on carbon steel studied by in situ AFM and electrochemical methods," *Industrial & Engineering Chemistry Research* 53 (2014): pp. 5858-5865.
14. H. Wang, B. Brown, S. Nestic, A. Pailleret, "In Situ Atomic Force Microscopy Study of Microstructure Dependent Inhibitor Adsorption Mechanism on Carbon Steel," *CORROSION 2022*, paper no. 17739 (San Antonio, TX: AMPP 2022).
15. H. Wang, S. Sharma, A. Pailleret, B. Brown, S. Nestic, "Investigation of corrosion inhibitor adsorption on mica and mild steel using electrochemical atomic force microscopy and molecular simulations," *Corrosion* 78 (2022): pp. 978–990.
16. J.D. Olivo, B. Brown, D. Young, S. Nestic, "Effect of Corrosion Inhibitor Alkyl Tail Length on the Electrochemical Process Governing CO<sub>2</sub> Corrosion of Mild Steel," *Corrosion* 75 (2019): pp. 137-139.
17. H. Wang, B. Brown, S. Nestic, A. Pailleret, "Investigation of Organic Inhibitor on Mild Steel using In Situ Atomic Force Microscopy and Electrochemical Measurement," *CORROSION 2020*, paper no. 14792 (NACE 2020 digital conference proceedings).
18. G. Xie, J. Ding, B. Zheng, W. Xue, "Investigation of adhesive and frictional behavior of GeSbTe films with AFM/FFM," *Tribology International* 42 (2009): pp. 183-189.
19. P. J. James, M. Antognozzi, J. Tamayo, T.J. McMaster, J.M. Newton, M.J. Miles, "Interpretation of contrast in tapping mode AFM and shear force microscopy. A study of nafion," *Langmuir* 17 (2001): pp. 349-360.
20. D. Polcari, P. Dauphin-Ducharme, J. Mauzeroll, "Scanning electrochemical microscopy: a comprehensive review of experimental parameters from 1989 to 2015," *Chemical Reviews* 116 (2016): pp. 13234-13278.
21. K. Singla, H. Perrot, B. Brown, S. Nestic, Adsorption of Model Inhibitor Compound Characterized Using Quartz Crystal Microbalance, Submitting to AMPP 2023 conference proceedings. Symposia: Corrosion Control with Inhibition between Oil and Gas, paper no. 19145.
22. J.D. Olivo, D. Young, B. Brown, S. Nestic, "Effect of corrosion inhibitor alkyl tail length on the electrochemical process underlying CO<sub>2</sub> corrosion of mild steel," *CORROSION 2018*, paper no.11537 (Houston,TX: NACE 2018) .
23. Y. He, S. Ren, Z. Belarbi, X. Wang, D. Young, M. Singer, M. Mohamed-Saïd, S. Camperos, "Micellization and Inhibition Efficiency," *CORROSION 2021*, paper no.16872 (Virtual Conference: AMPP 2021).
24. Y. He, S. Ren, X. Wang, D. Young, M. Singer, Z. Belarbi, M. Mohamed-Said, S. Camperos, M.R. Khan, K. Cimatu, "Delinkage of Metal Surface Saturation Concentration and Micellization in Corrosion Inhibition," *Corrosion* 78(2022): pp. 625-633.